



Intrinsic optical properties of Ag-doped poly-(vinyl alcohol) nanocomposites: an analysis of the film thickness effect on the plasmonic resonance parameters

Corentin Guyot¹ · Michel Voué¹

Received: 13 July 2020 / Accepted: 4 October 2020 / Published online: 17 October 2020
© Springer-Verlag GmbH Germany, part of Springer Nature 2020

Abstract

The optical properties of silver nanoparticles originating from the collective oscillations of their conduction electrons (LSPR) play a major role in the development of nanotechnology-based optical devices, from optical sensors to bactericide materials via non-linear optical devices. In this study, nanocomposites polymer films embedding silver nanoparticles were prepared by thermal annealing of poly-(vinyl alcohol) films doped by silver nitrate using a “one-pot synthesis” method. In this upscalable solution-based process, the nanoparticles are directly grown in the polymer matrix, yielding a plasmonic nanocomposite with a high density of nano-objects. Low (2.5% w:w) and high (25% w:w) doping concentration of silver were considered as well as their effect on the optical properties of thin (30 nm) and thick (300 nm and more) films. The topography and the optical properties (refractive index n and extinction coefficient k) of such films were studied by atomic force microscopy and spectroscopic ellipsometry. Unexpectedly, for a given doping level, the parameters of the surface plasmon resonance (amplitude, position and width) were shown to be thickness-dependent. A multivariate statistical analysis technique was used to identify the differences in the optical behavior of thick and thin films.

Keywords Plasmonic nanocomposites · Spectroscopic ellipsometry · Silver nanoparticles · Multivariate analysis · Polymer films · Nanoparticles growth · Support vector machine

1 Introduction

Plasmonic nanocomposites (PNCs) belong to an emerging class of materials whose optical properties take advantage of the surface plasmon resonance of the metal nanoparticles (NPs) embedded in a dielectric matrix. They are highly customizable by tuning the nanostructures shape and size as well as the mechanical behavior (stiffness, flexibility, Young’s modulus) and physical properties (glass transition) of the matrix [1]. PNCs have numerous applications such as optical sensors, non-linear optical devices [2–5], biosensors or bactericide materials [6–10]. The study of their

optical properties is an active research field and is driven by the interest for the Localized Surface Plasmon Resonance (LSPR). Well-known in its effect since e.g. the optical aspect of the Lycurus cup (4th CE) or of the mosaics of Saint Sabina (5th CE) [11], the LSPR appears when free electrons of the metal are excited by the electromagnetic field associated to the propagation of light [12, 13]. The most popular way to prepare these PNCs is the “bottom-up” approach: metal NPs are synthesized in colloidal solutions and stabilized with or without further specific coating to prevent their aggregation. In this synthesis, several experimental factors can provide a considerable control of the formation of NPs. However, to produce PNCs, the NPs in the colloidal solution have to be dispersed and immobilized in a dielectric matrix such as glass or polymer (see e.g. [14–17] and the references therein). This approach has therefore two separate steps: the synthesis of the NPs and their dispersion in the matrix.

Another upscalable solution-based process is to grow the NPs directly in the polymer matrix. This is the process retained for our study. According to this “one-pot” synthesis method, a noble metal salt (AgNO_3 , in our case) is directly

✉ Michel Voué
michel.voue@umons.ac.be
Corentin Guyot
corentin.guyot@umons.ac.be

¹ Research Institute for Materials Science and Engineering, Physics of Materials and Optics, University of Mons, Mons, Belgium

mixed with a polymer. This approach leads to a high concentration of NPs in the material [18]. The basic principle of the *in situ* methods is the use of one of the matrix components as a reducing agent of a metal salt and to speed-up the reduction of the metal cations *in situ* by irradiating or thermally annealing the solid phase. Polymers such poly(vinyl) alcohol (PVA) are excellent host materials for metal or semiconductor NPs [19] because they play the role of reducing agent but also contribute to the stabilization of the NPs. In the polyols method, the reduction step of the silver cations uses electrons originating from the -OH groups of the PVA molecules (Fig. 1a). Depending on the temperature, cross-linking of the polymer matrix can also be induced, reducing the solubility of the composite (Fig. 1b) [20]. However, in the case of polymer-based PNCs, the reproducibility of the NPs distributions in size and shape remains difficult to achieve and slight variations in the experimental conditions leads to different results evidenced by modifications of the plasmon resonance band parameters. Moreover, the detailed mechanism linking the optical properties of the nanocomposite to their structural parameters is today not fully understood although still being the subject of an increasing number of publications.

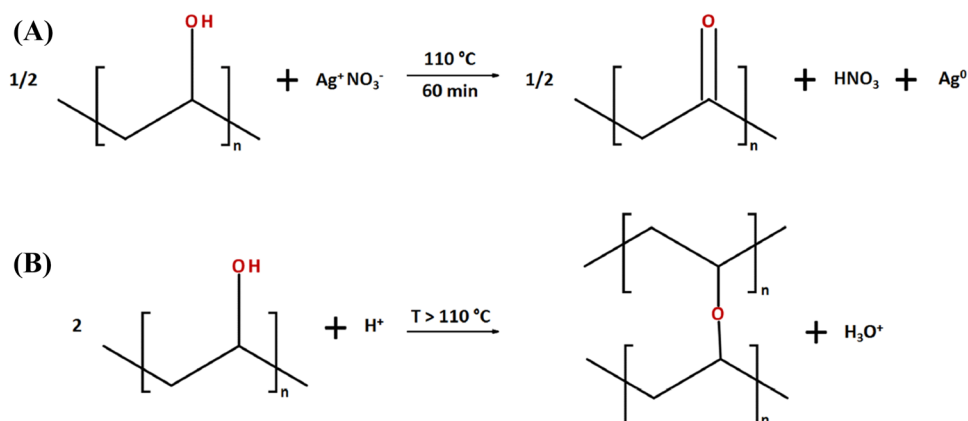
A large number of publications has been devoted to the study of the optical properties of NPs in solutions, considering the effects of solvent, temperature synthesis, surfactants, ... but much less authors have considered the growth of the NPs in a polymer film. Concerning the experimental technique, the optical properties of PNCs are usually probed using reflection or transmission spectrophotometry in the UV-visible spectral range. In our previous publications, we used spectroscopic ellipsometry (SE) [21, 22] or imaging ellipsometry (IE) [18, 23] to study the optical properties of Ag- or Au-doped PVA films produced by thermal annealing. As explained hereinafter, this optical analysis has the advantages of being non-destructive

and, moreover, of allowing the simultaneous determination of the film thickness and of its complex refractive index values. To date, only a reduced number of studies have been carried out using SE as an analysis technique [21, 22, 24–26]. Extensive reviews have been recently published by Oates, Wormeester and Arwin on spectroscopic ellipsometry studies of plasmon resonances at metal-dielectric interfaces of thin films and metallic nanostructures [27, 28].

As previously mentioned, interest for the Ag/PVA PNCs lays in the possible applications of their optical enhancing properties [29–31]. Some articles have been devoted to the study of the role of the polymer matrix [32] or of the chemical nature of the metal salt [33, 34]. The effects of annealing time and temperature have also been intensively studied (see e.g. [35–38]). On the contrary, the influence of the thickness of the film has only been considered in very few references [39] and most of the time a systematic study of its influence was not carried out. Moreover, the intrinsic optical properties of the nanocomposite is usually only considered to be a function of the optical properties of the metal and of the polymer and of their volume fraction.

In this article, we report in details on the influence the film thickness and on the silver doping of the PNCs on the plasmon resonance parameters. More precisely, we compare the resonance parameters in thin (less than 50 nm) and thick films (more than 300 nm) at a given Ag-doping level. We will show how, starting from the same silver-to-polymer mass ratio, nanocomposites with different refractive index can be obtained by simply tuning the film thickness. More precisely, the statistical distribution of the plasmon resonance parameters will be analyzed by multivariate statistics leading to the conclusion that at a given Ag⁺ doping level, thin and thick films behave differently. This effect is probably related to the growth process of the NPs in films with different thickness.

Fig. 1 **a** Reduction scheme for the silver cations and **b** Cross-linking of the PVA chains at high temperature (redrawn from [20])



2 Materials and methods

2.1 Nanocomposite film preparation

Polymer films were prepared according to the experimental procedure described in our previous publications [21, 22] and based on the original protocol of Porel and coworkers [40, 41]. A 10% (w:w) poly(vinyl alcohol) solution in MilliQ water was prepared as a stock solution (PVA, MW = 13,000–23,000, 98% hydrolyzed, Sigma-Aldrich). Dissolution of the polymer was achieved by heating the solution at 85°C. AgNO₃ (99.99%, Sigma-Aldrich) was added to the polymer solution after cooling to room temperature to obtain a silver concentration of 2.5% or 25%. Percentage corresponds to the w:w silver-to-polymer ratio. Required amount of water was added to the polymer stock solution to obtain 2% and 8% polymer solutions.

A small volume ($\approx 400 \mu\text{L}$) of the polymer solution containing the Ag⁺ cations was spin-coated on piranha-cleaned silicon wafers fragments (< 100 >, ACM, France). Silicon substrates were chosen because of their high optical contrast with polymer films and their low intrinsic roughness. Depending on the coating conditions, the final thickness of the dried film ranged from 18–25 nm (2% PVA, 60 s at 6000 rpm) to 300 nm and above (8% PVA, 60 s at 1600 rpm). After being dried in open-air atmosphere, the coatings were annealed 60 min at 110°C. Contrary to the case of glass substrates in which, by increasing the temperature, the coatings became yellowish-brown in color, in the case of silicon substrates, the color of the samples is mainly dominated by the interferometric color and the contribution of the plasmon resonance to the color change can hardly be seen by naked eyes. For comparison, reference PVA films were prepared according to the same method but omitting the AgNO₃ in the polymer solution.

Four types of samples were prepared by varying the film thickness ('T': thick ; 't': thin) and the doping level in silver ('H': high (25%) ; 'l': low (2.5%)). In the following, these categorical variables will be referred to as the class of the sample ('TH', 'Tl', 'tH' or 'tl') (Table 1).

2.2 Surface topography characterization

The topography of the films was studied by AFM (Park XE70, Park Systems Corp., Korea). The AFM operated in the air in intermittent contact mode with commercial ACTA tips (resonance frequency: 309 kHz). Areas of $5 \mu\text{m} \times 5 \mu\text{m}$, $2 \mu\text{m} \times 2 \mu\text{m}$ and $1 \mu\text{m} \times 1 \mu\text{m}$ were imaged for every sample. The resolution of the images was 256 pixels \times 256 pixels. The data were processed with the Gwyddion 2.53 software (<http://gwyddion.net/>) [42].

Table 1 Coating conditions for the four types of samples (Coating time: 60 s)

Samples ID	Polymer conc. (%)	Ag/PVA mass ratio (%)	Coating speed (rpm)	Approx. thickness (nm)
TH	8	25	1600	300
Tl	8	2.5	1600	300
tH	2	25	6000	30
tl	2	2.5	6000	30

2.3 Ellipsometry

The ellipticity of the samples was measured using a SOPRA GES5E rotating polariser spectroscopic ellipsometer with a 1024 channels CCD spectrograph allowing fast and accurate measurements in the range 1.37 to 4.96 eV. The angle of incidence (AOI) was set to 70 deg. and the ellipsometer operated in parallel beam configuration (beam small axis : 4 mm). SE results were processed using the SOPRA Winelli II software.

2.4 Multivariate statistical analysis

The multivariate analysis of the data was achieved using the *R* statistical software [43]. The *e1071* package [44] was used to carry out the classification tasks of the resonance peaks parameters.

3 Results and discussion

3.1 Surface topography of the nanocomposite

The topography of the surface was measured by AFM in intermittent contact mode after the annealing of the film at 110°C during 60 min. Figure 2a, b represent the topography and phase images ($1 \mu\text{m} \times 1 \mu\text{m}$) of a typical 30 nm-thick film. The mass ratio of Ag/PVA was 25% (w:w). The nanoparticles of silver were clearly observed by a variation of the phase value, which provides a local information of the nature of the nanocomposite, and a local variation of the height. In Fig. 2c, d, we represented the topography and the phase images corresponding to a 300 nm-thick film at the same Ag/PVA ratio. Figure 3 presents the AFM images (topography and phase) of the control films. They don't show a structuration at the nanoscale. The height and the phase values are normally distributed. The surfaces are smooth.

A first observation of these images of Fig. 2 shows that the size of the particles near the surface is influenced by the thickness of the film even if the silver-to-polymer weight ratio is kept constant. Figure 4 represents a boxplot of the radii r of the particles as determined from the AFM

Fig. 2 Topography (left) and phase (right) AFM images of Ag-PVA film doped with 25% AgNO₃ (w:w). **a, b** \approx 30 nm-thick film; **c, d** \approx 300 nm-thick film. Image size: 1 μ m \times 1 μ m (256 \times 256 pixels)

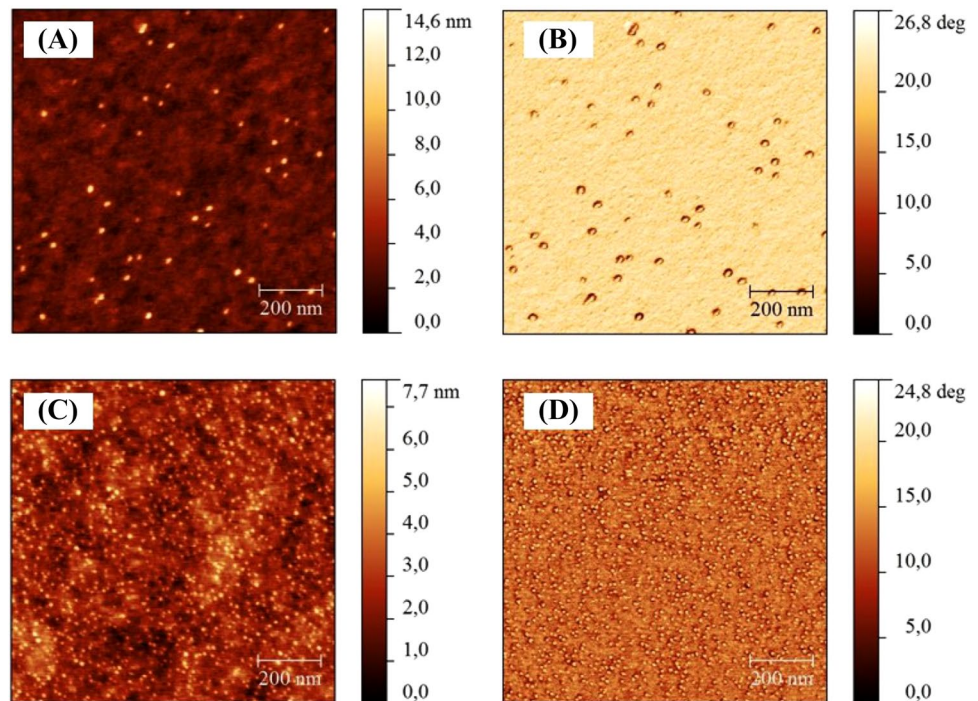
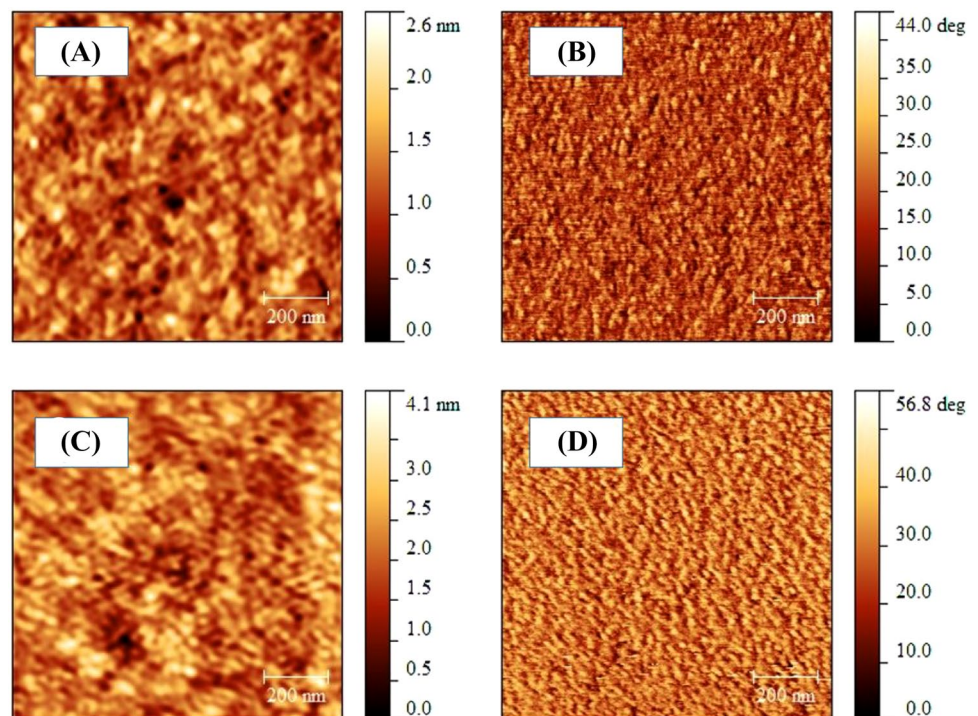


Fig. 3 AFM topographic (left) and phase (right) images of the PVA control films. **a, b** 30 nm-thick films **c, d** 300 nm-thick films. Image size: 1 μ m \times 1 μ m (256 \times 256 pixels)



images. The radii were corrected for the embedding of the spherical particles in the matrix following $r = (r_{eq}^2 + h^2)/(2h)$ where r_{eq} is the apparent radius of the particles and h the height emerging from the polymer matrix. The mean values are 8.2 ± 2.4 nm and 4.0 ± 2.5

nm for the 25 nm (*tH*) and 300 nm-thick (*TH*) films respectively. The whiskers corresponds to the interquartile range (IQR). According to this nanoscale analysis, it is clear that the particles embedded at the surface of the thick samples are smaller than the particles in the thinner ones.

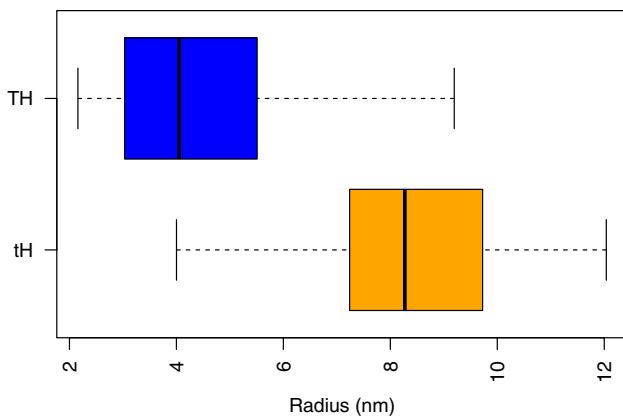


Fig. 4 Box-and-whiskers plots of the radius of the particles (Ag/PVA ratio: 25%; film thickness: 30 nm ('tH') and 300 nm ('TH'))

The roughness of doped and non-doped representative samples was characterized by the average surface roughness parameter (S_a) and by the root-mean-square surface roughness parameter (S_q) [45]. The measurements show a significant difference between doped and non-doped film in both cases (thick or thin films) (Table 2). As seen from both the S_a and the S_q surface roughness values, the growth of the nanoparticles induced by the annealing of the film controls the roughness of the surface, although it remains quite low (≤ 1 nm).

3.2 Optical properties

The purpose of this study was to compare the optical properties of thick and thin films embedding AgNPs grown *in situ* from the same polymer solution. To that purpose, we prepared a series of nanocomposite films on a glass substrate and investigated the onset of the LSPR peak as a function the annealing time (Sect. 3.2.1).

To compare the optical responses of the PNCs, optical models are required to calculate the complex refractive index of the layers from SE measurements, i.e. from the Ψ and Δ spectra. This second part of the study was achieved by preparing nanocomposite films on silicon substrates which are known to be more convenient for an ellipsometric study due to the high optical contrast between the substrate and the doped polymer film (Sect. 3.2.2).

Table 2 Roughness parameters of the doped (Ag/ PVA = 25%) and undoped (pure PVA) films

	Thick film		Thin film	
	Doped	Undoped	Doped	Undoped
S_a (nm)	0.66	0.40	0.59	0.32
S_q (nm)	0.85	0.52	0.77	0.42

3.2.1 Absorbance in the UV-VIS range

In the first series of experiments, the optimum annealing time range of the samples was determined by measuring the evolution with the annealing time of the height of the LSPR peak. These measurements were carried out using a Genesys 20 UV-Vis spectrometer (Thermo, USA). To that purpose, cleaned glass substrates were coated with the PVA 8% solution at a 25% Ag/PVA mass ratio and annealed at 110°C. The annealing time was varied from 10 to 60 min and the spectra were recorded from 300 to 800 nm. The reference spectrum was measured on an uncoated glass substrate. As expected the plasmon resonance was observed slightly above 415 nm and the position of the peak did not significantly vary with the annealing time (Fig. 5).

As shown in Fig. 6, the absorbance stabilizes after 40 to 50 min, suggesting the complete reduction of the Ag^+ ions. The fluctuations are due to the changes in thickness from one sample to the other. The absence of a significant shift in the LSPR peak position shows that, in a first approximation, the average size of the AgNPs does not significantly vary.

3.2.2 Spectroscopic ellipsometry

Spectroscopic ellipsometry (SE) is a widely used optical analysis technique based on the change of polarization of light after reflection of an incident light beam on a substrate or on a stratified sample [46, 47]. Due to its non-destructive nature, SE is a powerful technique to analyze at once the optical properties of materials and the thickness of the different layers of the sample. More specifically, one measures at a given wavelength the ellipticity ρ which is defined by

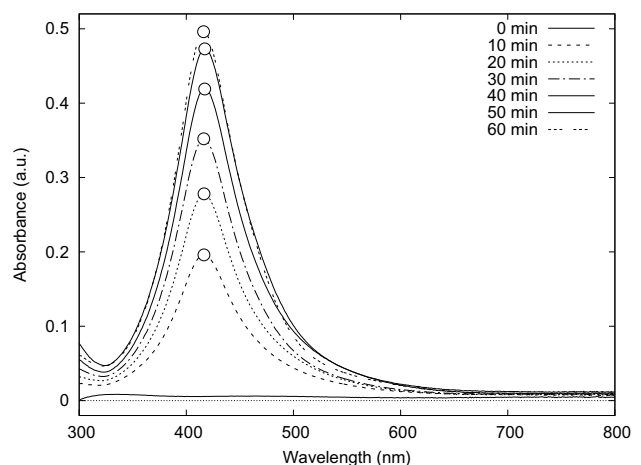


Fig. 5 Absorbance spectra of a characteristic series of AgPVA films as a function of their annealing time ($T = 110^\circ C$, Ag/PVA mass ratio: 25%, film thickness ≈ 400 nm). No significant change in the LSPR peak position is observed ($\lambda_0 = 416.6 \pm 0.4$ nm, open circles)

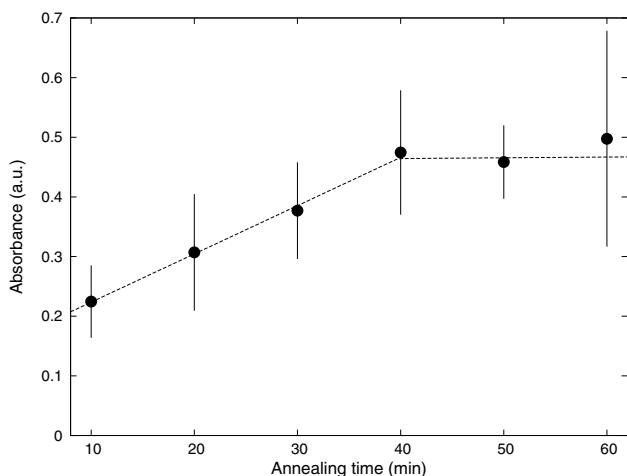


Fig. 6 Evolution with the annealing time of the absorbance at the resonance (Annealing temp.: 110°C - Data point: median, Error bars: interquartile range, number of replica: 8, dashed lines: weighed regression lines)

$$\rho = \frac{r_p}{r_s} = \tan \Psi e^{i\Delta} \tag{1}$$

where r_p and r_s are the complex reflectance coefficients of the p - and s -components of the incident light, respectively. Ψ and Δ are the ellipsometric angles. They are explicitly defined by

$$\tan \Psi = |r_p|/|r_s| \quad \text{and} \quad \Delta = \delta_p - \delta_s \tag{2}$$

where δ_p and δ_s are the phase-shifts undergone by the p - and the s -components of the incident wave during the reflection. The angle Δ therefore measures the relative phase-shift between the perpendicular components of the propagating light wave. Except in a very limited number of cases, Ψ and Δ cannot be directly converted into the refractive index and/or film thickness. Indeed, the ellipticity is a complex

quantity which is a function of the angle of incidence, of the optical properties of the materials and of the thickness of the layers. Taking into account the dispersion of the dielectric function, Eq. 1 has to be inverted in most cases using numerical methods, assuming specular reflection of light at ideal planar interfaces. Contrarily to the UV-VIS spectrophotometric measurements [48, 49], reflection, absorption and transmission of light are considered at once in a SE measurement.

3.2.3 Modeling of the optical properties

The models used to interpret the SE data are described hereinafter and illustrated in Fig. 7.

PVA layer: A one-layer Cauchy model was chosen to represent the optical properties of the PVA films in the transparent range ($k_{PVA}(\lambda) = 0$)

$$n_{PVA}(\lambda) = A_{PVA} + \frac{B_{PVA}}{\lambda^2} \tag{3}$$

Ag-PVA layer: To the Cauchy model described above, a Lorentzian oscillator was added to account for the localized absorption of the plasmon resonance in visible range [47]. The specific contribution of the plasmon resonance to the wavelength-dependent complex dielectric function $\epsilon(\lambda)$ is given by

$$\epsilon(\lambda) = \epsilon_r(\lambda) + i\epsilon_i(\lambda) \tag{4}$$

$$\epsilon_r(\lambda) = \epsilon_\infty + \frac{A\lambda^2(\lambda^2 - A_0^2)}{(\lambda^2 - A_0^2)^2 + \Gamma_0^2\lambda^2} \tag{5}$$

$$\epsilon_i(\lambda) = \frac{A\lambda^3\Gamma_0}{(\lambda^2 - A_0^2)^2 + \Gamma_0^2\lambda^2} \tag{6}$$

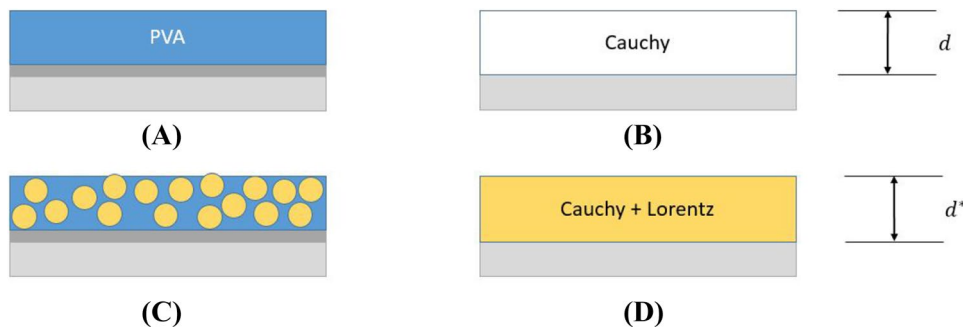


Fig. 7 Schematic representation of the optical models used to interpret SE data: **a** PVA layer on silicon, **b** Cauchy model used to describe the optical properties of the PVA layer, **c** AgNPs in PVA layer on Si and **d** a Cauchy model and Lorentzian oscillator used to

describe the optical properties of AgNPs in PVA matrix. Shaded area between the polymer layer and the substrate in a) and c) schemes: native SiO₂ layer. (2 nm, not to scale)

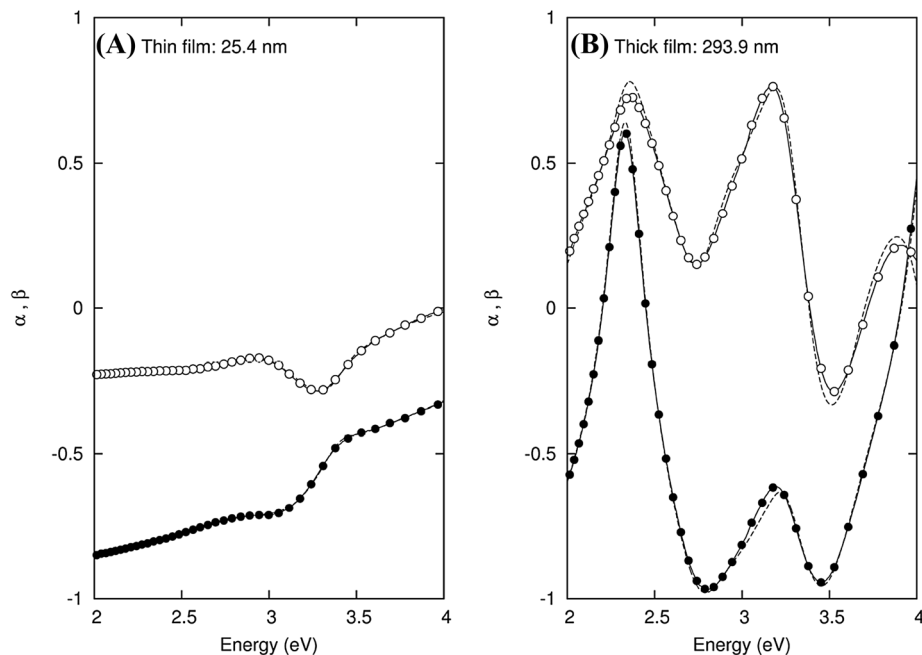
where λ denotes the wavelength. A_0 is the resonance wavelength of the oscillator, A its oscillator strength (i.e. amplitude of the resonance) and Γ_0 its full-width at half maximum (FWHM) and is hereinafter referenced to as the ‘width’ of the resonance. ϵ_∞ represents the contributions to ϵ_r from the resonances at wavelengths much greater than the measurable frequency range.

One of the main advantages of SE over conventional spectrophotometric methods is that it allows in most cases a simultaneous determination of the optical properties and of the thickness of the layers and not only the measurement of absorption or of transmission spectra. Figure 8 represents the SE data corresponding to a 25.4 nm-thick film (Fig. 8a) and to a 293.9 nm-thick film (Fig. 8b). Instead of representing the Ψ and Δ ellipsometric angles, we have chosen to present the $\alpha = \cos(2\Psi)$ and $\beta = \sin(2\Psi) \cos(\Delta)$ Fourier coefficients, which are closer to the experimental quantities measured by the ellipsometer. With respect to reference films of equivalent thickness, the ellipsometric data present spectra distortion in the 3.0–3.5 eV range. This is attributed to the localized plasmon resonance associated with the silver NPs. This effect is more noticeable for the thick films (Fig. 8b): one can see three peaks in the α -spectrum (filled symbols) but the second is considerably damped due to the energy absorption at the resonance. The data generated by the optimized optical model are also presented in Fig. 8 (dashed lines). They are in close agreement with the experimental data: the residual χ^2 values are respectively equal to $2.7 \cdot 10^{-4}$ and $2.9 \cdot 10^{-3}$ for the thin and thick films.

As previously described [21], to model the optical behavior of our samples, a one-layer Cauchy model was

chosen to represent the optical properties of the polymer matrix and a Lorentzian oscillator was added to account for the localized absorption of the plasmon resonance in the visible range. The use of the Cauchy model for the polymer matrix is justified by the monotonous increase of the refractive index of the polymer when going from the infrared to the UV, as expected for dielectric materials far from the fundamental absorption edge. The effect of the presence of the Lorentzian oscillator on the model is equivalent to using the Maxwell-Garnett effective medium approximation (MG-EMA) in a view of obtaining the dielectric function of the nanocomposite films [28, 50, 51]. One may expect our approach to be less dependent on the shape/size of the embedded NPs than the MG-EMA for which the depolarization factors linked to the particles shape have to be specified. Therefore, with our approach, two problems are implicitly solved: the dependence of the dielectric function of the silver NPs and the generalization of the MG-EMA to take into account the size and shape statistical distributions of the NPs. These two problems can easily be solved for spherical NPs [12, 26, 52] but require more complex approaches for non-spherical particles (see e.g. [13, 53, 54]). Moreover, these advanced models have to be supported by complementary experiments based e.g. on the quantitative analysis of transmission electron microscopy images to obtain the size distribution of the NPs. Also is avoided the influence of the doping level of the films: at high doping levels, it is expected that the nanocomposite films cannot be considered anymore as diluted solutions of NPs in a polymer matrix. The analysis of the optical response of

Fig. 8 Ellipsometric spectra of Ag nanoparticles-doped PVA films (Ag/PVA ratio: 25 % w:w): **a** ‘tH’ thin films (thickness: 25.4 nm); **b** ‘TH’ thick film (thickness: 293.9 nm). Experimental data: $\alpha = \cos(2\Psi)$ (filled circles) and $\beta = \sin(2\Psi) \cos(\Delta)$ (open circles). Dashed lines: optimized results from the optical model



nanocomposite films containing a high concentration of metal nanoparticles is more relevant of the metal island model [55, 56] which has been recently generalized by Wormeester and co-workers [57, 58]. Adding roughness or void inclusions did not significantly improved the quality of the fits, even for the thin samples.

The optical properties of the NPs-doped films are represented in Fig. 9a. For each type of film, the refractive index n and the extinction coefficient k of two different samples are represented to show the reproducibility of the analysis and indirectly, of the sample preparation. The presence of the silver NPs considerably modifies the optical properties in the doped polymer films: the presence of the absorption peak in the 2.5–3.5 eV range of the extinction coefficient spectrum (Fig. 9b) induces a large oscillation in the refractive index value (Fig. 9a) because of the Kramers-Krönig consistency of the optical properties and of the Lorentzian model of the peak. The perturbation of the refractive index occurs over the 1.5–4.5 eV range although the variation of the absorption peak is limited and the refractive index values are higher than the ones of a pure polymer film (see e.g. Fig. 5 in reference [22]). The optical properties of thin and thick films are clearly different as experimentally demonstrated here: starting from the same silver-to-polymer mass ratio, nanocomposites with different refractive index can be prepared by simply tuning the film thickness. The optimized parameters of the plasmon resonance peak are given in Table 3. In thin films, the amplitude of the resonance is higher, the position of the resonance smaller and the peaks wider than in thick ones.

Table 3 Typical parameters of the plasmon absorption peak (A : amplitude of the absorption peak; Λ_0 : position of the resonance; Γ_0 : width of the resonance) as a function of the film thickness for highly doped PVA films (Ag/PVA ratio: 25% w:w). Data correspond to the optical properties presented in Fig. 9

Sample	d (nm)	A ($\times 10^{-3}$)	Λ_0 (nm)	Γ_0 (nm)
Thin	23.4 ± 0.2	145 ± 6	414.2 ± 0.7	67.6 ± 2.9
	25.4 ± 0.3	133 ± 5	415.6 ± 0.6	69.0 ± 2.6
Thick	305.9 ± 1.7	117 ± 2	405.4 ± 0.7	47.3 ± 1.6
	293.4 ± 1.7	118 ± 2	409.5 ± 0.6	49.2 ± 1.5

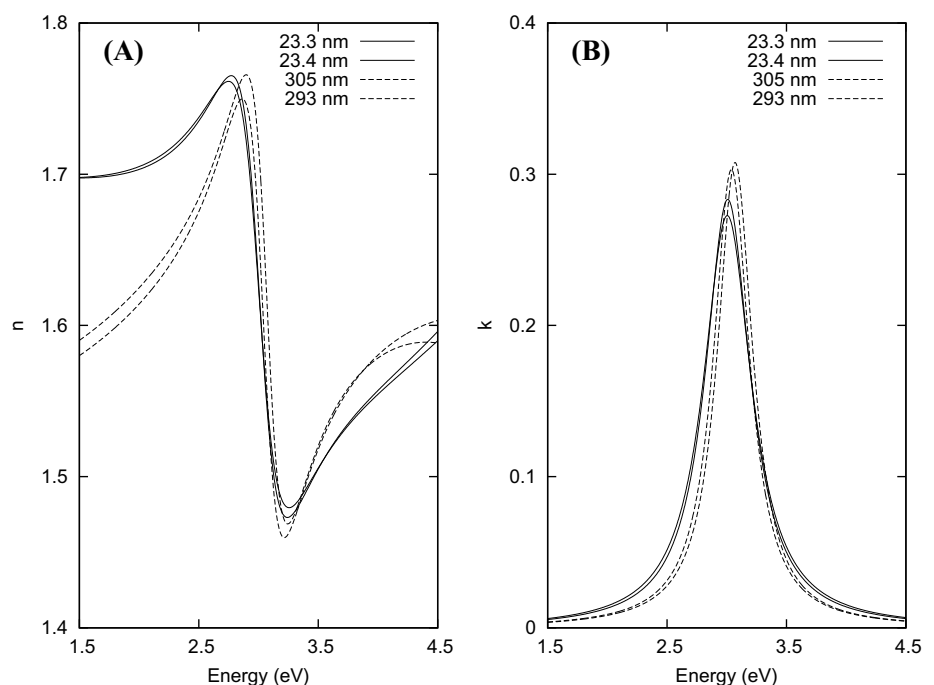
3.3 Multivariate analysis

Once the optical properties of the nanocomposites are determined and remembering that they are normally decorrelated from the thickness of the film, we considered the dispersion of the data cloud, the optical response of each nanocomposite being characterized by 3 parameters (A , Λ_0 and Γ_0) where A represents the oscillator strength or the amplitude of the resonance, Λ_0 correspond to the central resonance wavelength and depends on the size of the NPs, and finally where Γ_0 describes the width of the resonance and can be used to characterize the polydispersity of the NPs in the film. Statistical classes were defined on the basis of the thickness and doping of the samples (Table 4).

3.3.1 Data clouds of the resonance parameters

The samples considered for this study are distributed among 4 classes of relatively equivalent sizes. Each of the

Fig. 9 Optical properties of thin (plain lines) and thick (dashed lines) silver NPs-doped PVA films (Ag/PVA ratio: 25% w:w): **a**, refractive index n ; **b** extinction coefficient k



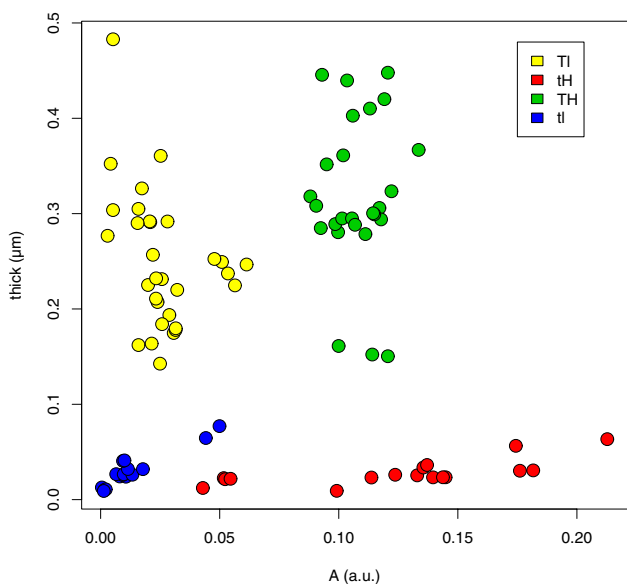


Fig. 10 Scatterplot of the thickness of the film (in μm) versus the strength of the oscillator. Color coding of the categorical variables are given in the legend and refer to Table 1

four classes are represented by a different color. Let us first consider the link between the thickness of the film and the strength of the plasmon band A (Fig. 10). One can easily see that the data cloud is subdivided into four areas, each of them being assigned to one type of nanocomposite. Samples with high doping level are on the right side of the plot with a higher value of the absorbance A in both case (thin and thick films, green and red symbols, respectively).

After this first analysis between the amplitude of the resonance and the thickness, it is interesting to plot the dispersion cloud for each pair of parameters, yielding a symmetric scatter plot matrix (Fig. 11). In the $\Lambda_0 - A$ and $\Gamma - A$ plots, different behaviors can be identified between the PNCs prepared from solutions with a high AgNO_3 concentration (red and green circles) and those prepared from diluted AgNO_3 solutions (blue and yellow circles). However, it seems more complicated to separate samples from different categories in the same subcloud: for example, red and green symbols are overlapping in the right subcloud for both graphs.

On the contrary, in the $\Gamma_0 - \Lambda_0$ plot, all subclouds are strongly overlapping and the interpretation of the plot is rather more complicated. This complicated link between the width of the resonance and its position has already

Fig. 11 Scatterplot matrix of the resonance parameters. Colour coding of the categorical variables are given in the legend. Units for peak position (“ Λ_0 ” or Λ_0) and peak width (“ Γ ” or Γ_0) are micrometers

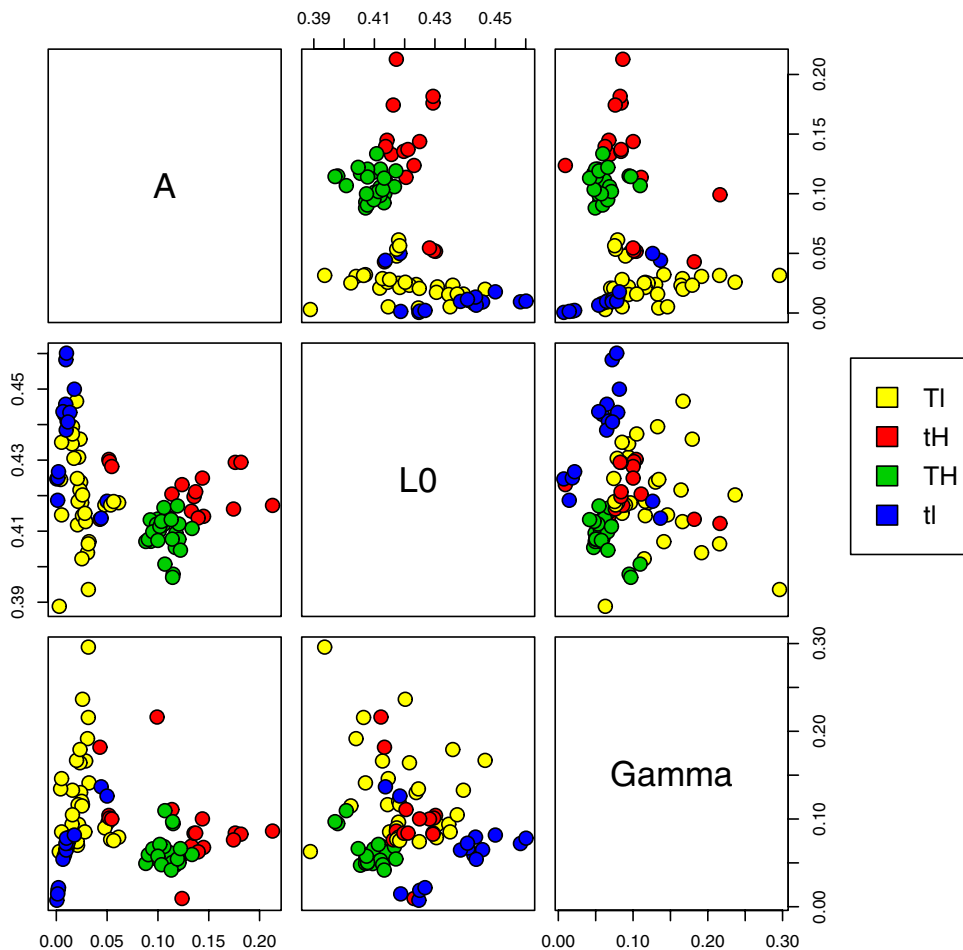


Table 4 Class sizes (N), means and standard deviations of the resonance parameters as a function of the nanocomposite type. Units for thickness, peak position (“ L_0 ” or Λ_0) and peak width (“ Γ ” or Γ_0) are nanometers

class	N	thickness (nm)	A (nm)	L_0 (nm)	Gamma (nm)
tH	17	28 ± 14	125 ± 50	421 ± 6	95 ± 46
TH	27	311 ± 82	102 ± 18	410 ± 5	64 ± 18
tl	16	30 ± 19	13 ± 14	437 ± 14	64 ± 36
TI	30	254 ± 76	28 ± 24	419 ± 15	127 ± 56

been considered by Berg and coworkers for mono- and polydispersed silver NPs in a glass matrix [59]. They observed a non monotonous variation. Starting from small particles (ca. 2 nm), an increase of the size of particles lead to a decrease of the FWHM and a blue shift of the position of the resonance peak until the radius of the particle has reached 10 nm. For larger particles, both FWHM and position of the resonance peak increase.

This global picture of the data cloud is reinforced by the statistical dispersion of the resonance parameters in terms of box-and-whiskers plots (Fig. 12).

As expected, the strength of the oscillator A is strongly dependent on the silver content of the film (Fig. 12a). Two trends emerge from the peak position dispersion: an increase of the amount of Ag^+ in the films ($l \rightarrow H$) blue-shifts the resonance peak. A decrease of the thickness of the films ($T \rightarrow t$) slightly red-shifts the resonance wavelength (Fig. 12b). This supports the fact that thickness plays an important role in the resonance parameters and therefore on the in situ synthesis of the AgNPs.

The evolution of the resonance width is more complicated (Fig. 12c). For example, increasing the film thickness ($t \rightarrow T$) leads to an increase of the FWHM for high doped samples and a decrease of FWHM for low doped samples. Looking at the decrease of the amount of Ag^+ ($l \rightarrow H$) leads to an increase of the FWHM for thick samples and a decrease of the FWHM for thin samples. By considering only the FWHM, it is complicated to draw a trend. For that reason, the behaviors of the films with low and high silver contents have to be separately considered in the remaining parts of this analysis.

3.3.2 Classification in the $\Gamma_0 - \Lambda_0$ plane

As we have seen from the scatter plot matrix and the box-and-whiskers plots, thick and thin films differently behave when we consider the resonance width (Γ_0) and the position of the plasmonic band (Λ_0). We, therefore, attempted to classify the films as a function of the silver content of the coated solution (2.5% or 25%). The classification task was performed for thin and thick films separately (Fig. 13) using support vector machines (SVM). They are statistical classification algorithms used to find the best classifier (i.e. separator) between two sets of (eventually overlapping) data points [60].

When the data are presented in the $\Gamma_0 - \Lambda_0$ plane, one can see that the set of data points corresponding to the highly doped films (circles) has only a slight overlap with the cloud of the films prepared from the 2.5% solution (triangles). To perform the classification task in a quantitative way, we used a SVM algorithm [44] derived from the original classification algorithm proposed by Vapnik [60]. In the case of

Fig. 12 Box-and-whiskers plots of the resonance peaks parameters: **a** peak height (A), **b** peak position (L_0) and **c** peak width (Γ). Categorical class definitions are given in the text. Colors in the online version

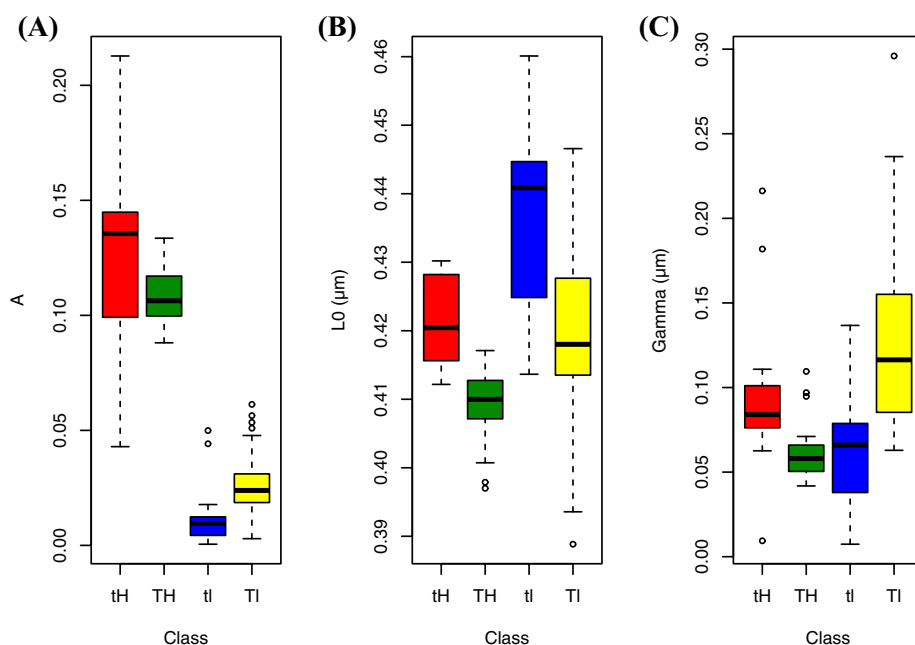
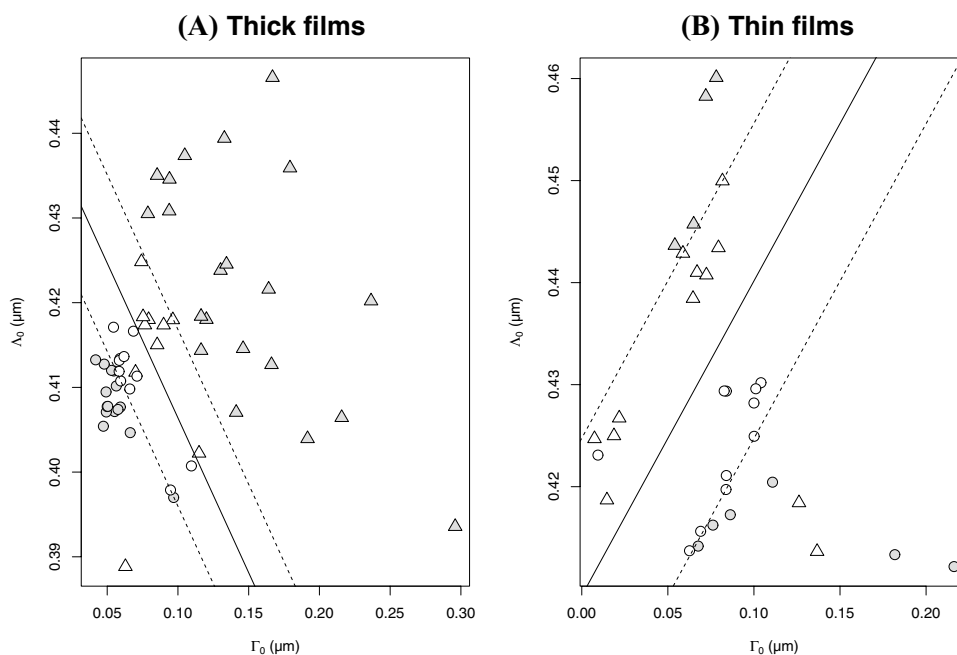


Fig. 13 Classification of the weakly and highly Ag-doped film in the $\Gamma_0 - \Lambda_0$ plane. **a** Thick films **b** Thin films (Ag-PVA ratio: 25% (circles) and 2.5% (triangles); Open symbols: support vectors; Lines: optimum classifier (plain) and margin (dashed)



overlapping data clouds, the classifier has to be tuned with respect to the penalty applied when an event is misclassified. Optimum results for the classifiers are represented in Fig. 13. The figure shows that, when applied to our data, SVMs allowed us to discriminate between the high- and low-doping level films in a very efficient way: only 3 films over 33 were misclassified in the thin films case and 3 over 54 in the thick films one. The most striking feature of the classification is the behaviour of the classifiers: when comparing panels (A) and (B) in Fig. 13, one can easily see that their slope have opposite signs. The classifiers slopes are respectively -0.36 (thick films) and $+0.30$ (thin films). The opposite sign in the slope of the separator confirm the difference in the optical behavior between thin and thick films in terms of position and width of the plasmon band.

3.4 Growth of nanoparticles

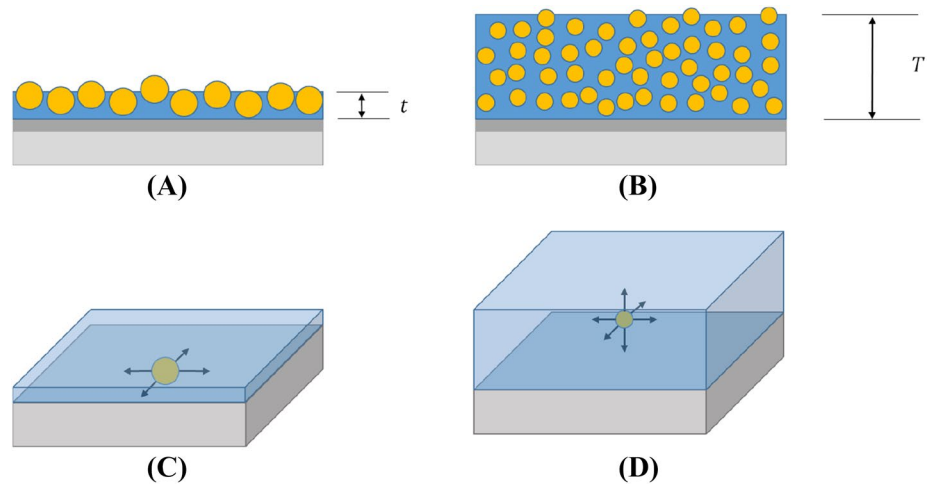
These different optical behaviours are probably strongly related to the growth process of the NPs in films of different thickness. We will discuss this point in the following paragraphs. Since the pioneer work of LaMer and Dinégar [61], the kinetics of growth of nanoparticles in solution has been the subject of an increasing number of publications and reported mechanism has been partially transposed to explain the growth of NPs in films. For both types of systems (films and solutions), one may expect the precursor solute to reach a critical level for nucleation. This prenucleation step is fed by the spatial distribution of the precursors (in our case, the Ag^+ ions) which we can consider to be isotropic within the film volume. As pointed out by Sugimoto [62], in films or sol-gel system, nucleation and growth of the generated

nuclei are separated due to the reduction of the supersaturation with the stabilization of the matrix, in contrast to the LaMer mechanism. In our case, it seems that, after the nucleation, the growth process is limited by the diffusion of Ag^+ ions or of the Ag^0 atoms in the film. The shape of AgNPs are spherical in both case (i.e. thin and thick films) but their sizes are different as clearly demonstrated in Fig. 4. A possible explanation of this different growth process can be associated with the diffusion process. In fact, in films whose thickness corresponds to a couple of NPs equilibrium diameter, NPs grow in a 2D-like matrix and the diffusion of silver ions is constrained in 2 dimensions by the substrate and the film/air interface. On the contrary, in thick films, the interfacial effect is expected to be less marked and the NPs rapidly form a 3D structure. The possible interpretation of the spatial distribution of the AgNPs is schematized in Fig. 14. A similar effect has been recently reported in Au – PVA films for which imaging ellipsometry shows local inhomogeneity of the optical response [18].

4 Conclusions

In summary, we have studied the surface topography and the optical properties of nanocomposite containing in situ grown silver nanoparticles. In particular, the study has been focused on the influence of the thickness of the film and of the silver concentration in the polymer matrix on the optical properties of the nanocomposite. We experimentally observed a different behaviour of thick and thin films as a function of the silver concentration. Topography and phase images of thin and thick nanocomposites were measured by AFM and

Fig. 14 Scheme of the NPs growth in **a** thin and **b** thick films. **c, d** represent the accessible dimensions for the diffusion process in thin (2D) and thick (3D), respectively



demonstrated that the size of the AgNPs seems to be larger in thin films than in thick films. The statistical distribution of the plasmon resonance parameters (A , A_0 and Γ_0), obtained by spectroscopic ellipsometry, has been analyzed using large margin classifiers. This multivariate analysis method leads to the conclusion that at a given Ag^+ doping level, thin and thick films behave differently, probably due to a different spatial distribution of the NPs in the polymer matrix limited by the diffusion process of ions or of the silver atoms in the film. This variation in the spatial distribution in thin and thick films is a possible explanation for the different behavior in the optical properties despite the fact that the diffusion process of ions in thin solid films still remains an open question.

Acknowledgements This work was supported by the Fonds de la Recherche Scientifique - FNRS under Grant nr 1926111.

References

- S.W. Hsu, A.L. Rodarte, M. Som, G. Arya, A.R. Tao, *Chem. Rev.* **118**, 3100 (2018)
- R. Kuladeep, L. Jyothi, S. Chakradhar, D. Rao, *Opt. Eng.* **53**, 071823 (2014)
- Y. Deng, Y. Sun, P. Wang, D. Zhang, H. Ming, Q. Zhang, *Physica E* **40**, 911 (2008)
- S. Anthony, S. Porel, D. Rao, T. Radhakrishnan, *Pramana J. Phys.* **65**, 871 (2005)
- X. Chen, J. Tao, G. Zou, Q. Zhang, P. Wang, *Appl. Phys. A Mater. Sci. Process.* **100**, 223 (2010)
- J.R. Morones, J.L. Elechiguerra, A. Camacho, K. Holt, J.B. Kouri, J.T. Ramirez, M.J. Yacaman, *Nanotechnology* **16**, 2346 (2005)
- N. Bhat, N. Karmakar, D. Kothari, *Int. J. Nanosci.* **12**, 1350029 (2013)
- A. Fuchs, S. Ritz, S. Pütz, V. Mailänder, K. Landfester, U. Ziener, *Biomater. Sci.* **1**, 470 (2013)
- T. Galya, V. Sedlarik, I. Kuritka, R. Novotny, J. Sedlarikova, P. Saha, *J. Appl. Polym. Sci.* **110**, 3178 (2008)
- N. Durán, M. Durán, M.B. de Jesus, A.B. Seabra, W.J. Fávaro, G. Nakazato, *Nanomed. Nanotechnol. Biol. Med.* **12**, 789 (2016)
- Y. Wei, H. Ebendorff-Heidepriem, J.T. Zhao, *Adv. Opt. Mater.* p. 1900702 (2019)
- U. Kreibig, M. Vollmer, *Optical Properties of Metal Clusters* (Springer, New York, 1995)
- D.D. Evanoff, G. Chumanov, *ChemPhysChem* **6**, 1221 (2005)
- K.L. Kelly, E. Coronado, L.L. Zhao, G.C. Schatz, *J. Phys. Chem. B* **107**, 668 (2003)
- C.J. Murphy, T.K. Sau, A.M. Gole, C.J. Orendorff, J. Gao, L. Gou, S.E. Hunyadi, T. Li, *J. Phys. Chem. B* **109**, 13857 (2005)
- X. Huang, S. Neretina, M.A. El-Sayed, *Adv. Mater.* **21**, 4880 (2009)
- C.J. Murphy, L.B. Thompson, D.J. Chernak, J.A. Yang, S.T. Sivapalan, S.P. Boulos, J. Huang, A.M. Alkilany, P.N. Sisco, *Curr. Opin. Colloid Interface Sci.* **16**, 128 (2011)
- C. Guyot, P. Vandestruck, I. Marenne, O. Deparis, M. Voué, *Beilstein J. Nanotechnol.* **10**, 1768 (2019)
- Z.H. Mbhele, M.G. Salemane, C.G.C.E. van Sittert, J.M. Nedeljković, V. Djoković, A.S. Luyt, *Chem. Mater.* **15**, 5019 (2003)
- L. Nicolais, G. Carotenuto, *Nanocomposites: In Situ Synthesis of Polymer-Embedded Nanostructures* (Wiley, Amsterdam, 2014)
- N. Dahmouchène, S. Coppée, M. Voué, J. De Coninck, *Physica Status Solid. C* **5**, 1210 (2008)
- M. Voué, N. Dahmouchène, J. De Coninck, *Thin Solid Films* **519**, 2963 (2011)
- C. Guyot, P. Leclère, M. Voué, *J. Vac. Sci. Technol. B* **38**, 013602 (2020)
- S. Kurbitz, J. Porstendorfer, K.J. Berg, G. Berg, *Appl. Phys. B Lasers. Opt.* **73**, 333 (2001)
- T. Oates, *Appl. Phys. Lett.* **88**, 213115 (2006)
- T. Oates, E. Christalle, *J. Phys. Chem. C* **111**, 182 (2007)
- T. Oates, H. Wormeester, H. Arwin, *Prog. Surf. Sci.* **86**, 328 (2011)
- H. Wormeester, T. Oates, in *Ellipsometry at the Nanoscale*, ed. by M. Losurdo, K. Hingerl (Springer, Berlin, 2013), chap. 6, pp. 225–256
- T. Baker, O. Monti, D. Nesbitt, *J. Phys. Chem. C* **115**, 9861 (2011)
- T. Jiang, J. Li, L. Zhang, B. Wang, J. Zhou, *J. Alloy. Compd.* **602**, 94 (2014)
- D. Whitcomb, B. Stwertka, S. Chen, P. Cowdery-Corvan, *J. Raman Spectrosc.* **39**, 421 (2008)
- R. Abargues, K. Abderrafi, E. Pedrueza, R. Gradess, J. Marqués-Hueso, J.L. Valdés, J. Martínez-Pastor, *New J. Chem.* **33**, 1720 (2009)
- O. Yeshchenko, I. Dmitruk, A. Dmytruk, A. Alexeenko, *Mater. Sci. Eng. B* **137**, 247 (2007)

34. C. Sun, R. Qu, C. Ji, Y. Meng, C. Wang, Y. Sun, L. Qi, J. Nanopart. Res. **11**, 1005 (2009)
35. G.V. Ramesh, S. Porel, T.P. Radhakrishnan, Chem. Soc. Rev. **38**, 2646 (2009)
36. G. Ramesh, B. Sreedhar, T. Radhakrishnan, Phys. Chem. Chem. Phys. **11**, 10059 (2009)
37. S. Clémenson, L. David, E. Espuche, J. Polym. Sci. Part A: Polym. Chem. **45**, 2657 (2007)
38. S. Clémenson, D. Léonard, D. Sage, L. David, E. Espuche, J. Polym. Sci. Part A: Polym. Chem. **46**, 2062 (2008)
39. S. Clémenson, P. Alcouffe, L. David, E. Espuche, Desalination **200**, 437 (2006)
40. S. Porel, S. Singh, S.S. Harsha, D.N. Rao, T.P. Radhakrishnan, Chem. Mater. **17**, 9 (2005)
41. S. Porel, N. Venkatram, D.N. Rao, T.P. Radhakrishnan, J. Nanosci. Nanotechnol. **7**, 1887 (2007)
42. D. Necas, P. Klapetek, Cent. Eur. J. Phys. **10**, 181 (2012)
43. R Core Team, *R: A Language and Environment for Statistical Computing*. R Foundation for Statistical Computing, Vienna, Austria (2012). <http://www.R-project.org/>. ISBN 3-900051-07-0
44. D. Meyer, E. Dimitriadou, K. Hornik, A. Weingessel, F. Leisch, *e1071: Misc Functions of the Department of Statistics (e1071)*, TU Wien (2014). <http://CRAN.R-project.org/package=e1071>. R package version 1.6-2
45. P. Klapetek, *Quantitative Data Processing in Scanning Probe Microscopy - SPM Applications for Nanometrology* (Elsevier, Amsterdam, 2012)
46. R.M.A. Azzam, N.M. Bashara, *Ellipsometry and Polarized Light* (North-Holland, Amsterdam, 1977)
47. H. Tompkins, E. Irene (eds.), *Handbook of Ellipsometry* (Springer, New York, 2005)
48. E.M. El-Menyawy, G.M. Mahmoud, R.S. Ibrahim, F.S. Terra, H. El-Zahed, I.K. El Zawawi, J. Mater. Sci. Mater. Electron. **27**, 10070 (2016)
49. S. Aziz, M. Rasheed, H. Ahmed, Polymers **9**, 194 (2017)
50. D.E. Aspnes, J.B. Theeten, F. Hottier, Phys. Rev. B **20**, 3292 (1979)
51. D.E. Aspnes, in *Ellipsometry at the Nanoscale*, ed. by M. Losurdo, K. Hingerl (Springer-Verlag, 2013), chap. 5, pp. 225–256
52. A.S. Keita, A.E. Naciri, Phys. Rev. B **84**, 125436 (2011)
53. J. Toudert, L. Simonot, S. Camelio, D. Babonneau, Phys. Rev. B Condens. Mater. Phys. **86**, 045415 (2012)
54. Y. Battie, A.E. Naciri, W. Chamorro, D. Horwat, J. Phys. Chem. C **118**, 4899 (2014)
55. J. Lekner, *Theory of Reflection of Electromagnetic and Particle Waves* (Martinus Nijhoff Publishers, Leiden, 1987)
56. D. Bedeaux, J. Vlieger, *Optical Properties of Surfaces* (Imperial College Press, London, 2002)
57. E.S. Kooij, H. Wormeester, E.A.M. Brouwer, E. van Vroonhoven, A. van Silfhout, B. Poelsema, Langmuir **18**, 4401 (2002)
58. H. Wormeester, E.S. Kooij, B. Poelsema, Phys. Rev. B **68**, 085406 (2003)
59. K.J. Berg, A. Berger, H. Hofmeister, Zeitschrift für Physik D Atoms Mole. Clust. **20**, 309 (1991)
60. C. Cortes, V. Vapnik, Mach. Learn. **20**, 273 (1995)
61. V.K. LaMer, R.H. Dinegar, J. Am. Chem. Soc. **72**, 4847 (1950)
62. T. Sugimoto, J. Colloid Interface Sci. **309**, 106 (2007)

Publisher's Note Springer Nature remains neutral with regard to jurisdictional claims in published maps and institutional affiliations.